Delft University of Technology

Passive film formation and corrosion resistance of laser-powder bed fusion fabricated NiTi shape memory alloys

Liu, Ming; Zhu, Jia Ning; Popovich, V. A.; Borisov, E.; Mol, J. M.C.; Gonzalez-Garcia, Y.

Important note
To cite this publication, please use the final published version (if applicable).
Please check the document version above.

Original Article

Passive film formation and corrosion resistance of laser-powder bed fusion fabricated NiTi shape memory alloys

Ming Liu [a,b,*], Jia-Ning Zhu [b], V.A. Popovich [b], E. Borisov [c], J.M.C. Mol [b], Y. Gonzalez-Garcia [b]

[a] Center for Advancing Materials Performance from the Nanoscale (CAMP-Nano), State Key Laboratory for Mechanical Behavior of Materials, Xi'an Jiaotong University, Xi'an, 710049, PR China
[b] Department of Materials Science and Engineering, Delft University of Technology, Delft, the Netherlands
[c] Peter the Great Saint-Petersburg Polytechnic University, Saint Petersburg, Russia

ABSTRACT

Electrochemical tests and surface analysis measurements were performed to study the corrosion behavior in a 0.9 wt.% NaCl solution at 37 °C of three NiTi shape memory alloys fabricated by laser-powder bed fusion (L-PBF). The passive film characteristics and corrosion resistance of L-PBF NiTi showed different features as a function of their preparation process settings. The passivation rate for L-PBF NiTi surfaces including defects, such as keyhole pores and cracks which showed high electrochemical activity accelerating the passivation reaction process, was higher in the early stages of immersion, but the corrosion resistance provided by such a rapidly formed passive film containing higher defect density is lower than that for an initially defect-free surface. The thickness of the passive film including a higher defect density does not necessarily relate to the corrosion resistance. The L-PBF NiTi prepared at a linear energy density of 0.2 J/m and volumetric energy density of 56 J/mm³ shows the least defects. Also, an outer Ti-rich and inner Ni-rich dense and corrosion protective passive film could be obtained for these L-PBF NiTi samples, which also results in a relatively low Ni ion release rate. A passive film model based on thickness, composition and defect density properties as a function of processing conditions is proposed to explain the difference in corrosion resistance of the various L-PBF NiTi.
© 2023 The Author(s). Published by Elsevier B.V. This is an open access article under the CC BY license (http://creativecommons.org/licenses/by/4.0/).

1. Introduction

Shape memory alloys (SMA) show favorable elastic and dimensional memory properties as well as a low elastic modulus, which enhances mechanical compatibility and compliance for application in the medical field [1–3]. Among most SMA, NiTi with near-equal atomic ratio has the advantage of high biocompatibility, corrosion resistance, low stiffness and good damping and shock absorption in addition to an unloading recovery strain up to 8%. It has been widely used in biomedical fields such as oral orthodontics, artificial tissues

or organs, orthopedics, internal stent and clinical interventional therapy [4,5].

As a passivating alloy, a passive film mainly containing TiO_2 can be formed on the NiTi surface in air and service environment to protect it from extensive corrosion [6,7]. However, the corrosive environment of NiTi in human body can be considered to be relatively aggressive and varies as a function of time. Microorganisms in oral saliva, different electrolyte constituents, local acidification of the media around implants and (cyclic) mechanical stresses may reduce the stability of their passive films resulting in an increased release rate of Ni ions, possibly leading to further environmental changes, allergic reactions and inflammation. Many corrosion studies of NiTi have reported that the corrosion resistance could be affected by many factors such as alloy microstructure, coatings, nature of the corrosive media, etc [8−11]. Mirjalili et al. [12] reported that NiTi did not show obvious pitting corrosion in artificial saliva. However, adding fluoride ions could significantly promote the pitting corrosion process and pre-passivation of NiTi could improve its corrosion resistance to some extent. Močnik et al. [13] showed that a low content of fluoride ions (0.024 mol/L) had no significant effect on the corrosion resistance of NiTi in artificial saliva. Under action of mechanical wear, the Ni ion release rate was 134 times that of the maximum allowable limit. Electrochemical corrosion and corrosion fatigue are the most common forms of corrosion failure of NiTi implanted in the human body [9,14]. Figueira et al. [15] found that the corrosion resistance of NiTi is better than that of 316L stainless steel and worse than that of Ti−6Al−4V in Hanks solution. Peng et al. [16] reported that the base metal of NiTi with single-phase austenite showed higher corrosion resistance than the fusion and heat affected zones: the corrosion resistance decreased slightly in the fusion zone, the heat affected zone became the weakest corrosion resistance zone by the precipitation of a poorly corrosion resistant R-phase which considerably reduced the corrosion potential.

The lower corrosion resistance of NiTi-SMA is usually solved by coating, etc., currently, the applicability of intricately shaped NiTi-SMA is severely limited due to its poor manufacturability [2,8]. Additive manufacturing (AM) can effectively avoid many challenges and drawbacks of traditional subtractive manufacturing and now has become one of the current advanced processing and manufacturing technologies with even further development potential in the near future [17−19]. Therefore, with the advantages and versatility of AM, it is possible to manufacture complex NiTi materials and structures. Zhong et al. reviewed the recent progress of NiTi manufacturing by selective laser melting (SLM) [20]. Exploratory studies have been conducted on SLM NiTi, which is shown to be challenging. High density preparation of NiTi by SLM to obtain good mechanical properties, but also within strict composition boundaries to enable appropriate phase transformation properties, is shown to be strenuous. At present, there are few studies on corrosion behavior of NiTi manufactured by AM in medical environment. Increasing laser energy input during AM manufacturing can reduce the grain boundary density in the material enhancing the corrosion resistance. Marattukalam et al. [21] studied the influence of laser power on the corrosion rate of NiTi in Ringer's

solution, and found that the corrosion rate of the sample decreased with the increase of laser power.

In our previous work [22], experimental validation has demonstrated that analytical models predicting melt pool dimensions and defect formation criteria can provide an accurate estimation and guide manufacturability of defect-free Nitinol alloys. The cracks and keyhole-induced pores formation phenomena were experimentally analysed. In this study, a series of most typical L-PBF NiTi microstructures with defect-free, cracks and keyhole-induced pores were prepared through laser-powder bed fusion process condition variation and their corrosion resistance were studied. The corrosion resistance of three L-PBF NiTi were studied by means of electrochemical techniques to identify the corrosion resistance under different preparation process conditions combined with surface analysis to further analyze the passive film composition and thickness upon immersion in a simulated human body fluid (0.9 wt.% NaCl). The results of present work could provide some technical support for the preparation of 3D-printing NiTi-SMA with excellent corrosion resistance.

2. Experimental

2.1. Material and sample preparation

Commercial NiTi (50.0 at% Ni) powder manufactured by gas atomization (TLS Technik GmbH, Bitterfeld, Germany) was used as the initial powder for L-PBF fabrication. The laser-powder bed fusion (L-PBF) NiTi were fabricated with various volumetric energy densities (E_v, J/mm^3). Based on our previous work, it was found that microstructural defects and features in NiTi can be tailored via applying different E_v [22]. To remain consistent with our previous work, the same sample types and their definitions were used in this work, namely: 1) A2 with 56 J/mm^3 representing a defect-free sample; 2) A4 with 87 J/mm^3 with cracking defects; and 3) A6 with 60 J/mm^3 showing keyhole induced pores. The detailed L-PBF processing parameters are shown in Table 1. The printed cylindrical samples (Φ 6 mm × 10 mm) were cut into circular sheets by electrical discharging machining (EDM), and were ground and polished to remove EDM damage. Then, samples with a Φ 6 mm × 3 mm and Φ 6 mm × 2 mm are used for electrochemical analysis and for surface analysis, respectively. One circular side of the electrochemical sample was connected with a conductor and conductive adhesive, and the rest was sealed with epoxy resin to establish a 0.28 cm^2 exposed area. Before the experiment, all samples were polished from grit 200

Table 1 − The L-PBF manufacturing parameters of NiTi.

Sample	A2	A4	A6
Laser power, W	250	250	250
Scanning velocity, mm/s	1250	800	500
Hatch distance, μm	120	120	140
Layer thickness, μm	30	30	60
Laser beam size, μm	80	80	80
Linear energy density, J/mm	0.2	0.3	0.5
Volumetric energy density, J/mm^3	56	87	60

to 2000 step by step with SiC sandpaper, cleaned and dried with alcohol and deionized water.

2.2. Electrochemical tests

The standard three-electrode system was used for electrochemical test. L-PBF NiTi samples were used as the working electrode, platinum plate (10 cm^2) as the counter electrode, and the reference electrode was a saturated calomel reference electrode (SCE). The solution used in the experiments was a physiological aqueous solution with mass fraction of 0.9 wt.% NaCl, which was prepared by analytical pure chemical reagent and deionized water. Electrochemical tests were performed on a Biologic VMP3 multi-channel electrochemical workstation. The open circuit potential (OCP) was continuously monitored for 168 h. The potentiodynamic polarization measurements were started upon stabilization of the OCP for 1 h of immersion. The scan range of the potentiodynamic polarization measurements was from −250 mV vs. OCP to the anodic range at a scan rate of 1 mV/s, the scan was stopped at an anodic current density of 1 mA/cm^2. The cyclic voltammetry test was carried out from −1.0 V$_{SCE}$ to 2.0 V$_{SCE}$ and then back to the initial potential. A total of 5 scan cycles were performed at a scan rate of 50 mV/s. Electrochemical impedance spectroscopy (EIS) measurements were carried out at OCP with a signal sine wave amplitude of 10 mV, the test frequency range was 100 kHz - 10 mHz. The test results were analyzed by ZsimpWin 3.5 software. The test frequency of Mott−Schottky was fixed at 1 kHz, the scan rate was 50 mV/s and the scan potential range was −1.0 V$_{SCE}$ to +1.5 V$_{SCE}$. All electrochemical tests were performed at least three times and representative results are shown. The electrolyte temperature for all electrochemical measurements was controlled at 37 ± 0.5 °C by a thermostatic water bath.

2.3. Auger electron spectroscopy analysis

The through-thickness composition of the passive films on three L-PBF NiTi samples after immersion in 0.9 wt.% NaCl solution for 7 days was analyzed by Auger electron spectroscopy (AES). A scanning Auger model PHI-700, Ulvac-PHI, Japan was used. The detection was based on general principles (GB/T 26533-2011) of AES analysis methods. A coaxial electron gun and CMA energy analyzer were used. The high voltage of electron gun was 5 kV and the energy resolution was 1‰. The incident angle was 30°, and the vacuum degree of the analysis chamber was <3.9 × 10^{-9} Torr. The surfaces of the passive films were etched by Ar$^+$ ions with a Φ100 nm spot to obtain the depth profiles, the sputtering rate was 1 nm/min, determined by the thermal oxidation of a SiO$_2$/Si standard.

2.4. X-ray photoelectron spectroscopy analysis

The passive film composition of three L-PBF NiTi samples after immersion in 0.9 wt.% NaCl solution for 7 days was analyzed by X-ray photoelectron spectroscopy (XPS). For the analysis, the monochromator was Al Kα, the sensitivity was 100 kcps, the energy spectrum scanning range was 0−1350 eV, the wide scanning interval and narrow scanning interval was 1 eV and 0.1 eV respectively, and the energy spectrum was calibrated by C1s (285.0 eV). Element composition and content were analyzed by comparison with standard element spectra from Perkin-Elmer's XPS Data Sheet and XPS International Inc. Web site. Through analysis of the outer and inner passive film composition of L-PBF NiTi, the composition and structure of their passive films difference were further studied. Xpspeak 4.1 software was used to analyze data by Gauss-Newton fitting method.

2.5. Ni ion release test

The Ni ion release rate of three L-PBF NiTi samples after immersion in 0.9 wt.% NaCl solution for 7 days was analysed by Inductively Coupled Plasma Mass Spectrometry (ICP-MS). During the immersion, all samples were sealed to obtain an exposed area of 0.28 cm^2, and the samples were immersed in a glass beaker with 100 mL 0.9 wt.% NaCl solution. The Ni ion concentration was measured by ICP-MS type NexION 350D, USA, the corresponding wavelength of Ni is 233.7 nm.

3. Results and discussion

## 3.1. Microstructure and surface morphology

Optical micrographs of L-PBF NiTi fabricated with various volumetric densities E_v are shown in Fig. 1. From the top view (Fig. 1(a−c)), the grain width gradually grows with increasing E_v and even larger than the laser track distance (yellow markers in Fig. 1 (c)), which indicates an enhanced epitaxial grain growth. In contrast, interlocked grains could be observed in A2 sample (Fig. 1(a)) (E_v = 56 J/mm^3), and this type of grain morphology results in a better cracking resistance than A4 (Fig. 1(b)) (E_v = 87 J/mm^3) and A6 (Fig. 1(c)) (E_v = 60 J/mm^3). From the cross-sectional view, A2 consists of inter-stacking conduction melt pools (Fig. 1(d)), which shows defect-free quality. For A6 sample, the main defect type is keyhole-induced porosity. Since applying the relatively high linear energy density (E_l = 0.5 J/mm) in A6, keyhole mode melt pools were formed. When melt pools in the keyhole mode are present, pores are easily formed due to elemental evaporation and trapped gas. With further increasing E_v to 87 J/mm^3 and decreasing E_l to 0.3 J/mm (A4), cracking became the main defect type (Fig. 1(c, f)). The reason can be attributed to the relatively high residual stress associated with the high extent of thermal shrinkage during L-PBF. More detailed formation mechanisms of cracking and keyhole induced porosity can be found in our previous work [22], however its effect on electrochemical behavior should still be investigated. As shown in XRD patterns of L-PBF NiTi patterns measured at room temperature (Fig. 2), the main phase is B19' martensite for all samples and only tiny peaks are indexed as B2 austenite phase. It indicates that the consistency of phases among samples, which makes it reasonable to compare the effect of defects on corrosion behavior of L-PBF NiTi.

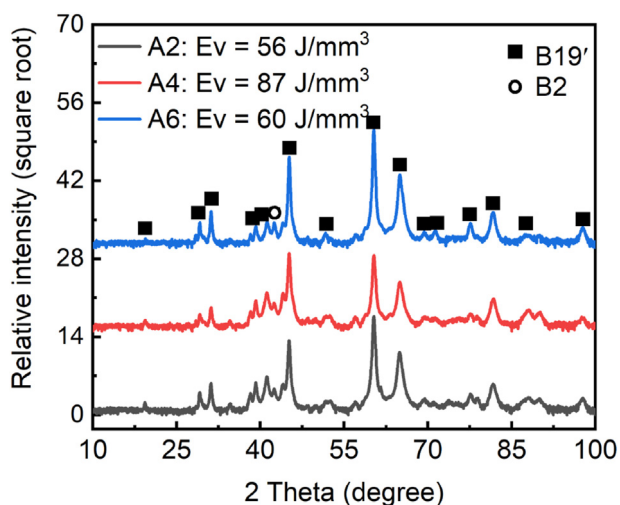## 3.2. Electrochemical analysis

3.2.1. Open circuit potential

The formation rate of the passive film in the early stages of exposure can be characterized by the OCP variation [23,24].
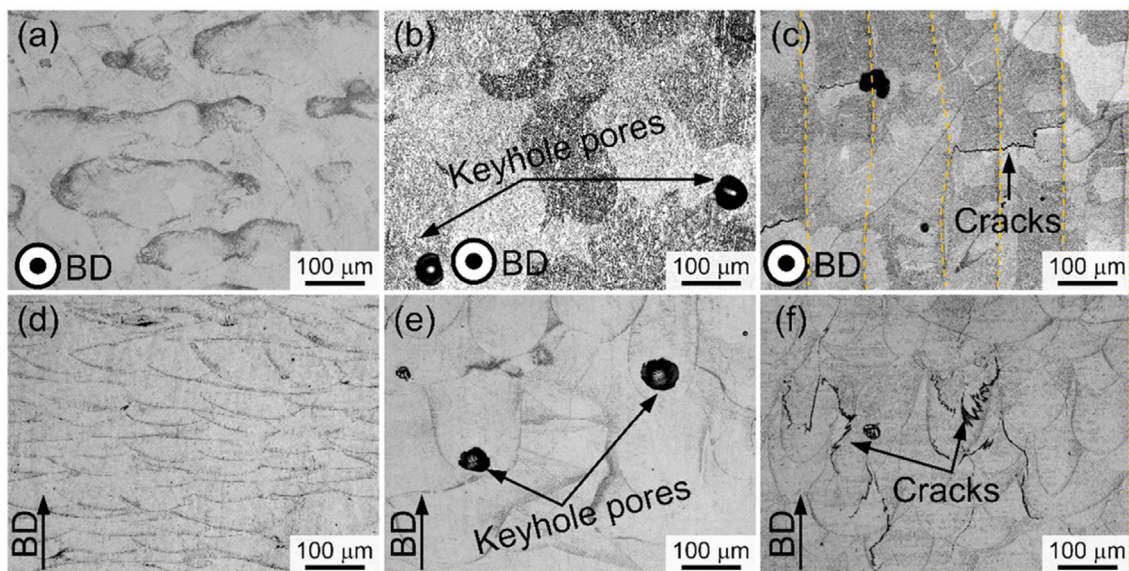
Fig. 1 − Optical micrographs for the L-PBF NiTi fabricated with different volumetric energy densities: (a, d) A2 (56 J/mm³), (b, e) A4 (87 J/mm³), and (c, f) A6 (60 J/mm³).

Fig. 2 − XRD patterns of L-PBF NiTi samples. A2 (56 J/mm³), A4 (87 J/mm³) and A6 (60 J/mm³).

Fig. 3 shows the OCPs of three L-PBF NiTi after immersion in 0.9 wt.% NaCl solution for 30 min. It can be seen that the OCP values of the L-PBF NiTi increase rapidly, but at different rates. The formation rate of the L-PBF NiTi passive films can be determined [23]:

$$E = \text{const.} + 2.303 \, \delta^- / A \log t \qquad (1)$$

where δ^- is the passive film growth rate at logt, A is a constant which can be calculated by the following equation [25]:

$$A = \frac{nF}{RT} \alpha \delta' \qquad (2)$$

where α is the charge transfer coefficient, ($\alpha = 0.5$) [24], and δ' represents the energy accumulation width during charge transfer, $\delta' = 1$ [25]. Most studies conformed that the passive film of NiTi is mainly TiO_2 [6,7], our further results of XPS and

AES also confirm that the outer layer of passive films of the three L-PBF NiTi is mainly TiO_2, hence, the thickness of L-PBF NiTi passive film in 0.9 wt.% NaCl solution increases mainly through Ti^{4+} diffusion to the interface between Ti and oxygen. The value of n in Eq. (2) is 4 and the calculated A is 78 nm/V. Then the OCP values vs. t could be transformed into E vs. 1/logt (see Fig. 3(b)), hence the early stage passive film growth rate δ^- of three L-PBF NiTi can be calculated by Eq. (1). It can be seen from Fig. 1(c) that the early stage passive film formation rate from high to low is: A6 > A4 > A2.

In order to study the long term passive film formation process of L-PBF NiTi in 0.9 wt.% NaCl solution, the OCP value of three L-PBF NiTi samples was measured in 0.9 wt.% NaCl solution for 7 days, as shown in Fig. 4. It can be seen that the OCP values of the three alloys increase rapidly during the first 6 h immersion, and then stabilize. The OCP value of A2 shows an increase from $-252 \, mV_{SCE}$ (30 min) to $-104 \, mV_{SCE}$ (6 h) and then slowly decreases to stabilize at $-180 \, mV_{SCE}$ after immersion for 3 days. After immersion for 30 min, the OCP value of A4 increases to $-171 mV_{SCE}$ and then stabilizes at about $-126 \, mV_{SCE}$ for 6 h. After immersion for 3 days, the OCP value of A6 has increased to $-130 \, mV_{SCE}$ and then to $-119 \, mV_{SCE}$ for 6 h. After immersion for 30 min, the OCP of A6 is also changed slightly and finally stabilized at $-130 \, mV_{SCE}$. After immersion for 7 days, the stabilized OCP values of the three L-PBF NiTi samples ranges from A2 < A4 ≈ A6. It can be preliminarily judged that the three L-PBF NiTi can form a certain protective passive film in 0.9 wt.% NaCl solution [23,24] which will be subject of further study from here.

3.2.2. Potentiodynamic polarization measurements

As can be seen from the OCP results in Fig. 4, the OCPs of the three L-PBF NiTi need at least 72 h to be stable, Fig. 5 shows the potentiodynamic polarization curves of L-PBF NiTi immersed in 0.9 wt.% NaCl solution after stabilization for 72 h. The potentiodynamic polarization curves of three L-PBF NiTi show the characteristics of typical metal passivation with a wide
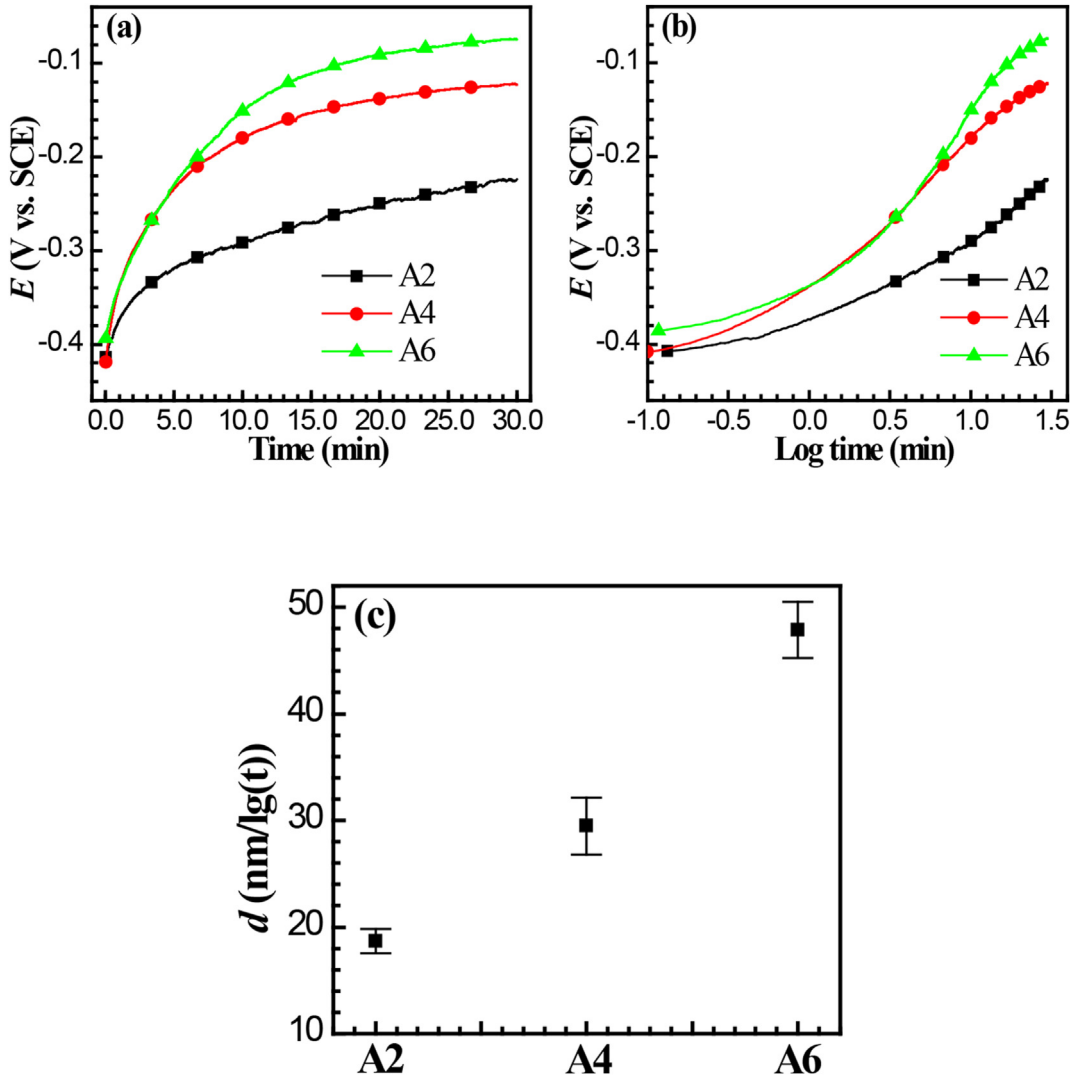
Fig. 3 − (a) OCPs of L-PBF NiTi after immersion in 0.9 wt.% NaCl for 30 min, (b) E vs. Logt (min), (c) passive film formation rate. A2 (56 J/mm³), A4 (87 J/mm³) and A6 (60 J/mm³).
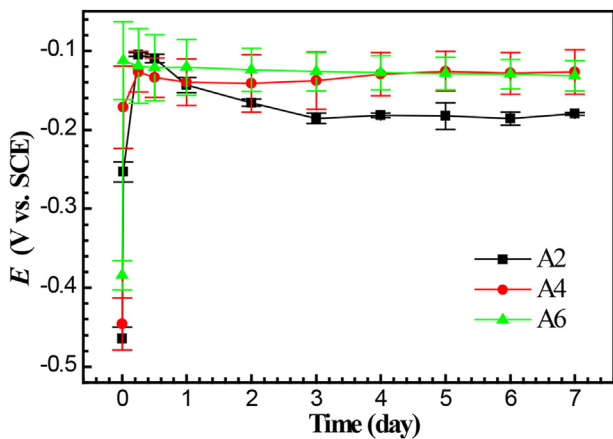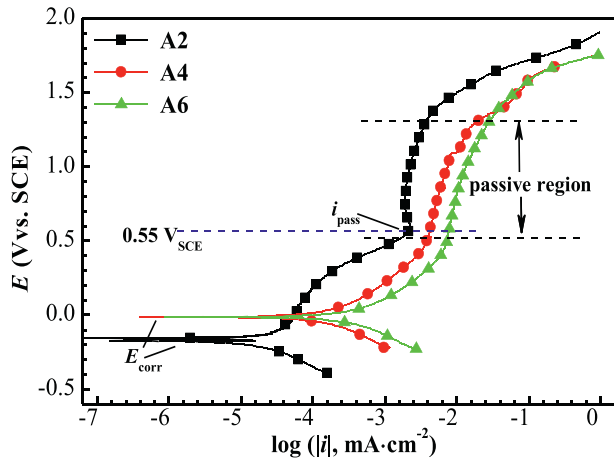

Fig. 4 − OCPs of L-PBF NiTi after immersion in 0.9 wt.% NaCl solution for 7 days. A2 (56 J/mm³), A4 (87 J/mm³) and A6 (60 J/mm³).

passive region [24]. The anodic polarization curves of L-PBF NiTi show a passivation region without obvious activation−passivation transition characteristics. The E_{corr} is the potential where the net current density of anode and cathode reaction is zero in the polarization curve, A2 has a relatively low E_{corr}, which is consistent with the OCP test results. In order to compare the passive current density (i_{pass}), the current density when the anode potential equals 0.55 V_{SCE} was used for comparison. The fitting results are listed in Table 2. The order of the passive current density (i_{pass}) and corrosion current density (i_{corr}) from low to high is: A2 < A4 < A6, the i_{corr} of A2 is less than 0.1 μA cm² indicating that a relatively well protecting passive film is formed [26].

3.2.3. Cyclic voltammetry

Fig. 6 shows the cyclic voltammetry curves of three L-PBF NiTi immersed in 0.9 wt.% NaCl solution. It can be seen from the wide range (−1.5 V_{SCE} - 2.0 V_{SCE}) and narrow range (−1.0 V_{SCE} -
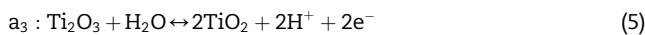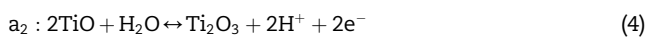
Fig. 5 — Potentiodynamic polarization curves of L-PBF NiTi after immersion in 0.9 wt.% NaCl solution for 72 h. A2 (56 J/mm³), A4 (87 J/mm³) and A6 (60 J/mm³).

Table 2 — Polarization curve parameters fitting values of L-PBF NiTi. A2 (56 J/mm³), A4 (87 J/mm³) and A6 (60 J/mm³).

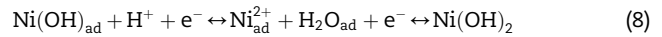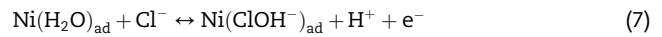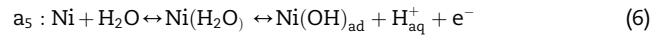| Sample	E_{corr}, (mV$_{SCE}$)	i_{corr}, μA cm^{-2}	b_a, mV dec^{-1}	b_c, mV dec^{-1}	i_{pass}, μA cm^{-2}
A2	-156 ± 10	0.02 ± 0.03	243 ± 12	-155 ± 12	2.1 ± 0.5
A4	-8 ± 12	0.21 ± 0.05	221 ± 13	-168 ± 13	4.4 ± 0.7
A6	-3 ± 14	0.52 ± 0.06	215 ± 10	-162 ± 11	7.3 ± 0.6

2.0 V$_{SCE}$) scanning curves of A2 in Fig. 6(a), five obvious anode current peaks could be observed, a_1 (-1.38 V$_{SCE}$) corresponds to the reaction of Ti to Ti^{2+}, a_2 (-1.1 V$_{SCE}$) corresponds to the transition from Ti^{2+} to Ti^{3+}, and a_3 (-0.59 V$_{SCE}$) corresponds to the transition from Ti^{3+} to Ti^{4+} [27]. The related reactions are [28]:

$$a_1 : Ti + H_2O \leftrightarrow TiO + 2H^+ + 2e^- \qquad (3)$$

$$a_2 : 2TiO + H_2O \leftrightarrow Ti_2O_3 + 2H^+ + 2e^- \qquad (4)$$

$$a_3 : Ti_2O_3 + H_2O \leftrightarrow 2TiO_2 + 2H^+ + 2e^- \qquad (5)$$

When the potential is positive at 0.6 V$_{SCE}$ and enter the oxygen control evolution process, two anodic current peaks (a_4 and a_5) could be observed. Three peaks could be seen in the back scanning curves, among which c_1 (1.25 V$_{SCE}$) is the reduction peak corresponding to a_4 and a_5, c_2 (-0.91 V$_{SCE}$) relates to the peak of a_3, and c_3 (-0.74V$_{SCE}$) is the reduction peak of a_2. The reduction reaction current of dissolved oxygen in water has reached the limit at -0.6 V$_{SCE}$ [26], and such strong current may cover part of the signal of the electrochemical reduction processes of Ti^{4+}/Ti^{2+}/Ti.

The cyclic voltammetry curves of A4 and A6 are similar in the wide potential range scanning (Fig. 6(b) and (c)), but after reducing the cathode scanning range to -1 V$_{SCE}$, small anodic current peaks (a_5) could be observed in A4 and A6 samples at about 0.3 V$_{SCE}$. The peak positions correspond to the transformation process from Ni to Ni^{2+} [29], which indicates Ni to be present in the passive film of A4 and A6 is unstable

compared with A2. A small Ni reduction current peaks (c_4) could also be seen in the back scanning curves, indicating that the generated Ni^{2+} will still remain in the inner layer of the passive film [30]. The possible reactions of Ni to Ni^{2+} in Cl$^-$ containing solution are as follows [31]:

$$a_5 : Ni + H_2O \leftrightarrow Ni(H_2O) \leftrightarrow Ni(OH)_{ad} + H_{aq}^+ + e^- \qquad (6)$$

$$Ni(H_2O)_{ad} + Cl^- \leftrightarrow Ni(ClOH^-)_{ad} + H^+ + e^- \qquad (7)$$

$$Ni(OH)_{ad} + H^+ + e^- \leftrightarrow Ni_{ad}^{2+} + H_2O_{ad} + e^- \leftrightarrow Ni(OH)_2 \qquad (8)$$

3.2.4.   Electrochemical impedance spectroscopy
In order to further identify the corrosion resistance and passive film formation process of L-PBF NiTi, the EIS with different immersion times were measured. Fig. 7 shows the representative Nyquist (Fig. 7(a)−(c)) and Bode (Fig. 7(a₁)-(c₁)) plots of L-PBF NiTi upon immersion in 0.9 wt.% NaCl solution for 0.5 h, 24 h and 168 h. It can be seen from the Nyquist plot that the arc of the capacitance loop of L-PBF NiTi increases slowly with immersion time. The Bode diagram of A2 shows two obvious capacitive arcs, indicating there are two time constants. With immersion time, the phase angle of A2 in the high frequency region (10^4-10^1 Hz) changes little, while the phase angle in the low frequency region (10^0−10^2 Hz) increases gradually. The Bode diagram of A4 changes little throughout the full immersion period, and its phase angle has a broad capacitive arc in the low-middle frequency range (10^3-10^1 Hz), indicating that there may be two superimposed time constants. The same as for A4, the Bode diagram of A6 also changes little, but two obvious capacitive arcs could be observed in the middle (10^3 Hz) and low frequency (10^1 Hz) regions, indicating that there are at least two time constants. The modulus of impedance $|Z|_{\omega \to 0}$ in the Bode plot is usually used to examine the charge transfer activity and hence the corrosion resistance of the alloy [32−34]. The $|Z|$ of L-PBF NiTi at 0.01 Hz is shown in Fig. 8 and shows that the value of $|Z|_{0.01}$ from high to low is: A2 > A4 > A6, indicating that A2 has the best corrosion resistance as compared to A4 and A6.

The previous electrochemical tests of potentiodynamic polarization (Fig. 5) and CV (Fig. 6) all demonstrate a passive film will be formed on the L-PBF NiTi, but according to the surface morphology analysis in Fig. 1, A4 and A6 samples have keyhole pores and crack defects, therefore, we adopt a defect-containing model to fitting the EIS data, the equivalent circuit used for EIS parameters fitting is shown in Fig. 8, which has also been used to study the corrosion behavior of NiTi and related alloys with defects in prior studies [15,35−37]. The model takes into account an inner oxide layer (R_b, Q_f) and an outer porous layer (R_p, Q_b), wherein, R_s is the solution resistance, R_p is the additional resistance of the solution inside the pores, Q_b is the pore wall capacitance, R_b is the barrier layer resistance, and Q_f is the barrier layer capacitance. The impedance of the equivalent circuit in Fig. 9 can be expressed by Eq. (9) [38]:

$$Z = R_s + \cfrac{1}{Z_{Q_f} + \cfrac{1}{R_p + \cfrac{1}{Z_{Q_b} + \frac{1}{R_b}}}} \qquad (9)$$

ZsimpWin 3.5 software was used to fit the EIS results, and the quality of the fitted parameters was evaluated by the chi-
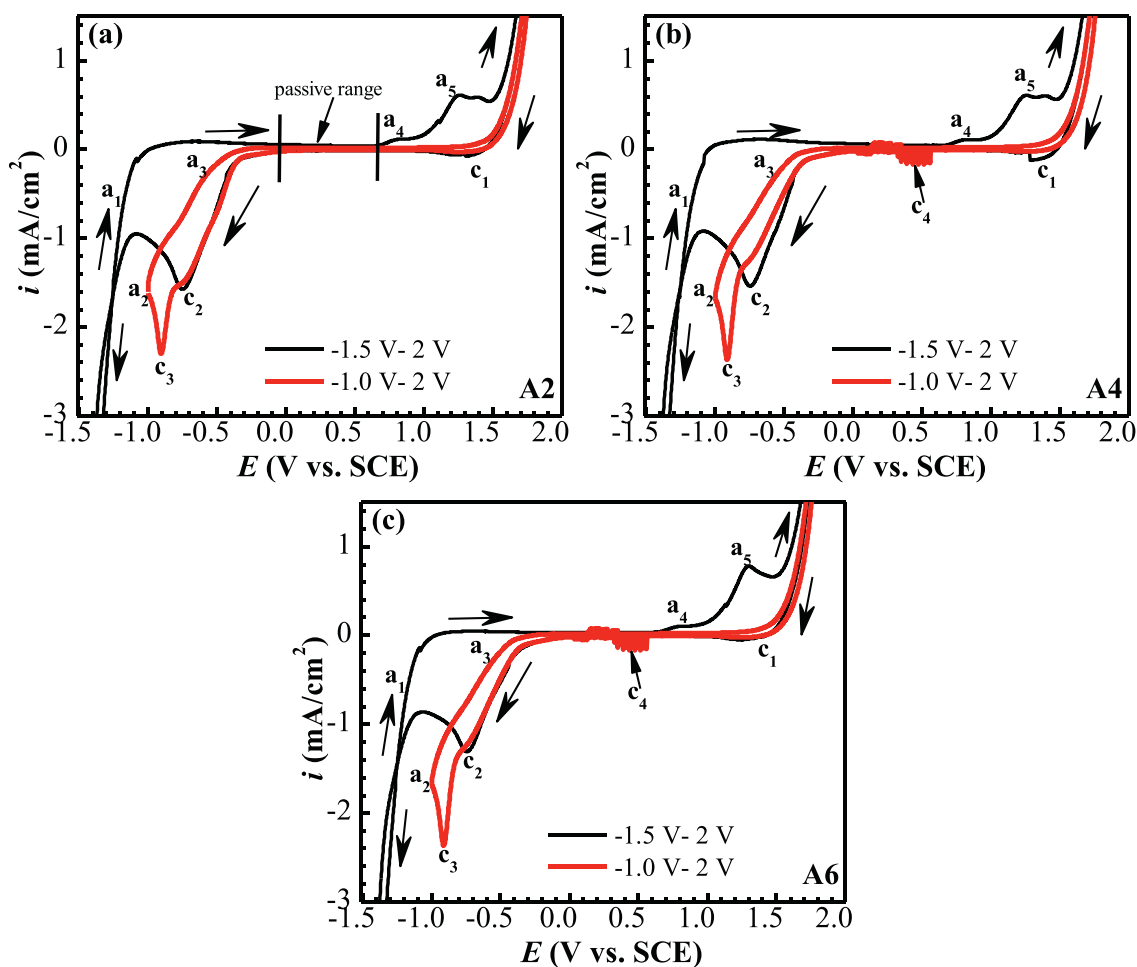
Fig. 6 – Cyclic voltammetry curves of L-PBF NiTi after immersion in 0.9 wt.% NaCl solution for 30 min. (a) A2 (56 J/mm³), (b) A4 (87 J/mm³), (c) A6 (60 J/mm³).

square value. In general, the capacitance is anon-ideal capacitor because of the roughness of the electrode surface [26,30]. The capacitance is related to the angular frequency of the excitation signal, which can be written as follows [39]:

$$Z_{Q_{dl}} = \frac{1}{Y_0(j\omega)^n} \tag{10}$$

where ω is the angular frequency, j is the symbol of an imaginary number, and n is the exponent of the constant phase element. n usually ranges from 0.5 to 1. When $n = 1$, the constant phase element is equivalent to the capacitance, the defect and the barrier layer (passive film) constant phase angle element Q_b and Q_f have similar meanings [15,36–39].

It can be seen from the fitting values in Tables 3–5 that the solution resistance R_s changes little, which is in the range of 8–13 Ω cm², the additional resistance of the solution inside the pores R_p (order 10^2–10^3 Ω cm²) is much smaller than that of R_b (order 10^4–10^5 Ω cm²). This indicates the corrosion resistance of R_p is smaller, which is consistent with the results reported by Figueira et al. [15], Chembath et al. [36], Freitag et al. [37] and Bolat et al. [40], their results all showed that R_p is usually within the order of 10^1–10^3 Ω cm² magnitudes. The good

fitness of the model to the data as shown in Fig. 7 corroborates the rationale to use the equivalent circuit (Fig. 9) to explain the corrosion process. Fig. 10 shows the fitted R_b variation with immersion time. The R_b of A2 increases from $10^{5.0}$ Ω cm² to $10^{5.8}$ Ω cm² after immersion for 30 min to 6 h, and then changes little in the subsequent immersion times; as for A4, R_b increases slightly from $10^{4.7}$ Ω cm² to $10^{4.9}$ Ω cm² after immersion for 30 min to 7 day; the R_b of A6 are in the $10^{4.8}$ Ω cm² order of magnitude and does not show any significant change after 30 min of immersion. It can be seen that corrosion resistance of the L-PBF NiTi in the whole 7 days from the high to low show the following order: A2 > A4 > A6. The corrosion resistance of A2 is comparable to that of the as-received NiTi alloys reported by Sun et al. [35], Figueira et al. [15], Chembath et al. [36] and Freitag et al. [37]. Our test environment is exactly the same as Sun's, their maximum R_b value of the dense NiTi alloy is 5.3×10^4 Ω cm², which is slightly higher than that for our worst sample A6 (4.0×10^4 Ω cm²), slightly worse than that for A4 (8.7×10^4 Ω cm²) and A2 (6.4×10^5 Ω cm²). The large difference in corrosion resistance of L-PBF NiTi could be related to the defects on their surface (see Fig. 1). A2 has the least defects, which may contribute to form a dense and stable
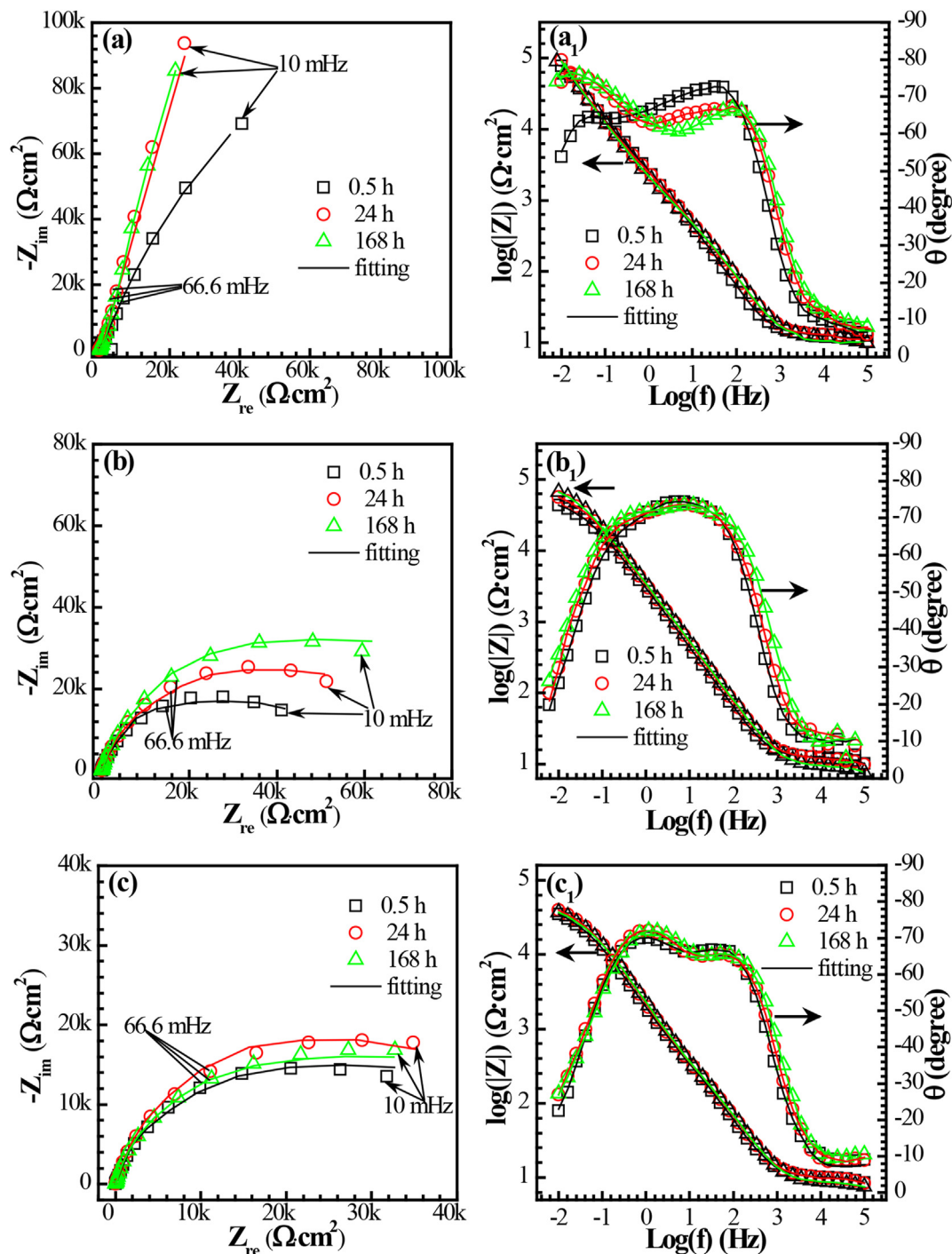
Fig. 7 — Nyquist (a), (b), (c) and Bode (a₁), (b₁), (c₁) diagrams of L-PBF NiTi after immersion in 0.9 wt.% NaCl solution for different times. (a), (a₁): A2 (56 J/mm³); (b), (b₁): A4 (87 J/mm³); (c), (c₁): A6 (60 J/mm³).

passive film. As stated in the OCP part (see Fig. 4), the defects could promote the formation rate of the passive film, but the rapidly formed passive film has a relatively poor corrosion resistance. Therefore, A4 and A6 could stabilize in a shorter period of time (30 min), but the corrosion resistance of their passive films are merely 10% of that A2.

The passive film barrier layer capacitance C_b can be calculated by the following equation [15,36–40].

$$C_b = Q_b^{1/n} R_b^{(1-n)/n} \tag{11}$$

It is assumed that C_b is related to the thickness of passive film [26], such as:

$$C = \varepsilon \varepsilon_0 A / d \tag{12}$$

where ε is the dielectric constant of the film oxide, the typical dielectric constant of TiO_2 is 100 [15], and ε_0 is the dielectric constant in vacuum, $\varepsilon_0 = 8.85 \times 10^{-12}$ F/m. A is the effective
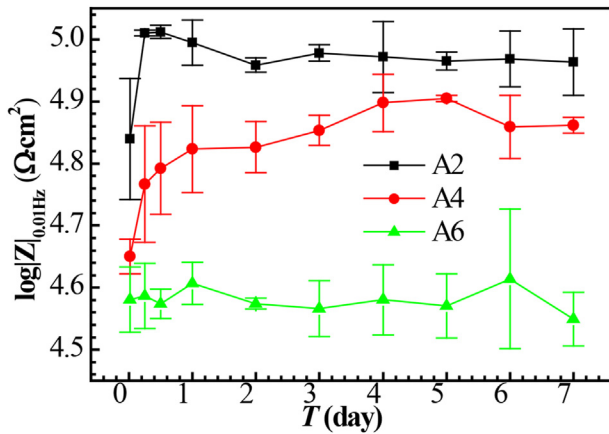
Fig. 8 – $|Z|_{0.01}$ of L-PBF NiTi after immersion in 0.9 wt.% NaCl solution for different times (0.5 h, 6 h, 12 h, 1 d, 2 d, 3 d, 4 d, 5 d, 6 d, 7 d). A2 (56 J/mm³), A4 (87 J/mm³) and A6 (60 J/mm³).

Fig. 9 – Equivalent circuit of L-PBF NiTi after immersion in 0.9 wt.% NaCl solution for different times.

area and d is the film thickness. Base Eq. (11), we calculate the thickness of the passive films of three L-PBF NiTi. The estimated passive film thickness of A2 is about 1 nm, A4 is 2–3 nm, and A6 is 2–3 nm, which is much lower than the reported 10 nm [6,7]. The apparent contradiction can be explained by the porous defect structure of the L-PBF NiTi passive film, and the actual working area may be much larger

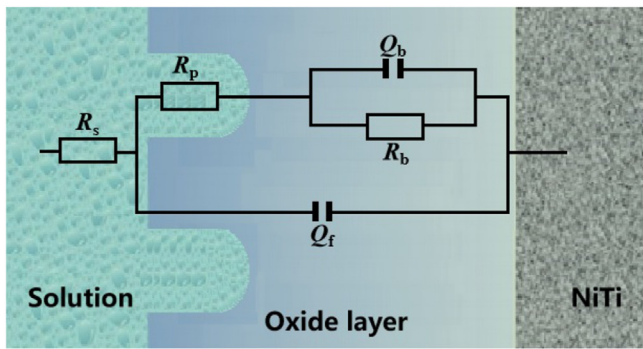than the geometric area considered in the calculation. Therefore, when the capacitance is constant, based on the relationship between C and d, the larger the passive film area, the higher the passive film thickness. According to the surface images analysis in Fig. 1, A2 has the least number of defects and thus has the smallest actual surface area. Therefore, it can be concluded that A2 may have the minimum passive film thickness. There may be non-positive correlation between the thickness and the corrosion resistance of passive film for the alloy with a high surface defect density.

3.2.5. Mott−Schottky analysis

Fig. 11(a) shows the Mott−Schottky curves of the three L-PBF NiTi immersed in 0.9 wt.% NaCl solution for 7 days. Based on classical semiconductor theory, Mott−Schottky Eq. (13) can be used to describe the linear relationship between $1/C^2$ and electrode potential [41,42]. When the electrode potential is higher than the flat band potential, the curves are all positive, indicating that the passive films of the L-PBF NiTi formed in 0.9 wt.% NaCl solution at OCP are n-type semiconductor, which again confirms the passive film on the NiTi surface is mainly composed of TiO_2 [41]. The donor carrier density in n-type semiconductors can be calculated based on Eq. (13) [26,42]:

$$\frac{1}{C^2} = \frac{2}{\varepsilon\varepsilon_0 eN_D}\left(E - E_{fb} - \frac{kT}{e}\right) \tag{13}$$

where C is the space charge layer capacitance of the oxide film; E is applied potential; ε_0 is the vacuum dielectric constantand, $\varepsilon_0 = 8.85 \times 10^{-12}$ F/m; ε is the dielectric constant of the passive film, the typical dielectric constant ε of titanium oxide is 100 [15], e is the quantity of electrons, $e = 1.602 \times 10^{-19}$ C; N_D is the electron donor concentration; E_{fb} is the flat band potential, which is the voltage intercept corresponding to the straight section of the M−S curve, k is the Boltzmann constant, $k = 1.38 \times 10^{-23}$ J/K; T is the thermodynamic temperature.

As can be seen from the fitting results in Fig. 11(b), the passive film defect concentration of the three L-PBF NiTi increases with the amount of their surface defects, and the carrier density in the passive films of A2, A4 and A6 is 1.31, 1.85 and 2.23 (10^{20} cm^{-3}), respectively. The number of defects in A6 passive film is 1.7 times more than that of A2, which again indicates that the A2 sample has the least defects and shows the highest corrosion resistance.

Table 3 – EIS parameters fitting values of A2 (56 J/mm³) after immersed in 0.9 wt.% NaCl solution for different times (0.5 h, 6 h, 12 h, 1 d, 2 d, 3 d, 4 d, 5 d, 6 d, 7 d).

Time, h	R_s, Ω cm²	Q_f, Y_0 Ω^{-1} cm^{-2} s^n	n	R_p, kΩ cm²	Q_b, Y_0 Ω^{-1} cm^{-2} s^n	n	R_b, kΩ cm²	chi-squared
0.5	13.2	6.0×10^{-5}	0.82	4.1	29.4×10^{-5}	1.0	118.3	1.7×10^{-3}
6	13.1	5.2×10^{-5}	0.87	4.0	18.2×10^{-5}	0.97	664.3	1.2×10^{-3}
12	12.9	5.6×10^{-5}	0.86	0.7	17.1×10^{-5}	0.96	650.2	1.3×10^{-3}
24	12.9	4.7×10^{-5}	0.87	1.2	17.9×10^{-5}	0.98	692.3	1.3×10^{-3}
48	12.3	11.1×10^{-5}	0.85	1.4	11.7×10^{-5}	0.84	681.1	1.1×10^{-3}
72	11.6	11.9×10^{-5}	0.83	1.3	11.6×10^{-5}	0.84	650.5	1.3×10^{-3}
96	11.5	9.3×10^{-5}	0.84	1.4	6.4×10^{-5}	0.83	622.1	1.1×10^{-3}
120	10.5	9.2×10^{-5}	0.74	1.3	8.5×10^{-5}	0.83	669.3	1.7×10^{-3}
144	10.8	9.8×10^{-5}	0.83	0.4	10.5×10^{-5}	0.84	656.3	1.7×10^{-3}
168	11.0	9.9×10^{-5}	0.83	0.4	11.9×10^{-5}	0.84	640.7	1.0×10^{-3}

Table 4 — EIS parameters fitting values of A4 (87 J/mm³) after immersed in 0.9 wt.% NaCl solution for different times (0.5 h, 6 h, 12 h, 1 d, 2 d, 3 d, 4 d, 5 d, 6 d, 7 d).

Time, h	R_s, $\Omega\,cm^2$	Q_f, Y_0 $\Omega^{-1}\,cm^{-2}\,s^n$	n	R_p, $\Omega\,cm^2$	Q_b, Y_0 $\Omega^{-1}\,cm^{-2}\,s^n$	n	R_b, $k\Omega\,cm^2$	chi-squared
0.5	9.4	5.4×10^{-5}	0.73	5.7	2.3×10^{-5}	0.95	52.7	2.2×10^{-4}
6	9.4	4.9×10^{-5}	0.75	5.4	1.9×10^{-5}	0.94	61.7	3.6×10^{-4}
12	8.3	4.1×10^{-5}	0.73	6.2	2.7×10^{-5}	0.91	65.0	2.5×10^{-4}
24	9.0	4.4×10^{-5}	0.75	6.0	2.2×10^{-5}	0.92	71.6	2.7×10^{-4}
48	9.2	4.3×10^{-5}	0.75	5.8	2.1×10^{-5}	0.92	80.6	2.8×10^{-4}
72	9.9	5.2×10^{-5}	0.86	6.2	1.5×10^{-6}	0.68	83.2	2.0×10^{-4}
96	9.0	5.8×10^{-5}	0.79	5.8	6.5×10^{-6}	0.99	92.2	1.8×10^{-4}
120	9.1	5.9×10^{-5}	0.80	6.6	5.0×10^{-6}	0.99	96.0	1.9×10^{-4}
144	8.7	5.7×10^{-5}	0.80	6.1	5.8×10^{-6}	0.99	82.0	2.1×10^{-4}
168	8.4	5.9×10^{-5}	0.80	6.2	4.5×10^{-6}	0.99	86.9	1.4×10^{-4}

Table 5 — EIS parameters fitting values of A6 (60 J/mm³) after immersed in 0.9 wt.% NaCl solution for different times (0.5 h, 6 h, 12 h, 1 d, 2 d, 3 d, 4 d, 5 d, 6 d, 7 d).

Time, h	R_s, $\Omega\,cm^2$	Q_f, Y_0 $\Omega^{-1}\,cm^{-2}\,s^n$	n	R_p, $k\Omega\,cm^2$	Q_b, Y_0 $\Omega^{-1}\,cm^{-2}\,s^n$	n	R_b, $k\Omega\,cm^2$	chi-squared
0.5	10.6	5.5×10^{-5}	0.87	1.2	3.1×10^{-5}	0.78	41.5	8.8×10^{-4}
6	10.2	5.4×10^{-5}	0.86	1.0	3.1×10^{-5}	0.78	40.6	7.0×10^{-4}
12	10.2	5.2×10^{-5}	0.86	1.0	3.0×10^{-5}	0.78	40.8	7.7×10^{-4}
24	10.2	5.3×10^{-5}	0.86	0.9	3.1×10^{-5}	0.78	43.6	8.6×10^{-4}
48	10.2	4.6×10^{-5}	0.87	0.4	4.3×10^{-5}	0.74	45.5	9.7×10^{-4}
72	9.8	4.5×10^{-5}	0.87	0.4	4.6×10^{-5}	0.73	39.2	1.7×10^{-3}
96	9.6	4.4×10^{-5}	0.87	0.3	4.7×10^{-5}	0.73	40.1	2.1×10^{-3}
120	9.4	4.3×10^{-5}	0.88	0.3	5.0×10^{-5}	0.71	39.9	2.1×10^{-3}
144	9.2	4.2×10^{-5}	0.88	0.3	5.3×10^{-5}	0.71	40.1	2.3×10^{-3}
168	9.0	4.1×10^{-5}	0.88	0.3	5.6×10^{-5}	0.70	39.9	2.6×10^{-3}
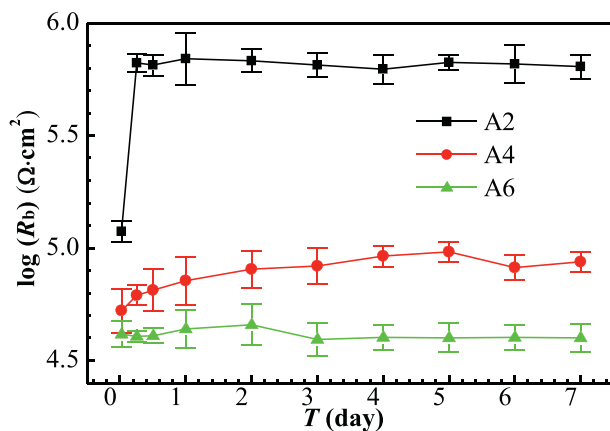
Fig. 10 — R_b of L-PBF NiTi after immersion in 0.9 wt.% NaCl solution for different times (0.5 h, 6 h, 12 h, 1 d, 2 d, 3 d, 4 d, 5 d, 6 d, 7 d), A2 (56 J/mm³), A4 (87 J/mm³) and A6 (60 J/mm³).

3.3. AES analysis

The AES results of L-PBF NiTi immersed in 0.9 wt.% NaCl for 7 days is shown in Fig. 12. With the increase of sputtering depth, the content of O decreases rapidly, the content of Ti increases slowly, and the content of Ni increases sharply and exceeds Ti at 5.4, 5.6 and 6.6 nm for A2, A4 and A6 respectively, indicating that outer layer of the L-PBF NiTi is mainly Ti- oxide and Ni is mainly enriched in the inner layer of the passive film. The thickness of the passive film is generally considered to be positioned at the location where the oxygen content is halved [43], which is 8.5, 9.8 and 13.8 nm for A2, A4 and A6 respectively. This is consistent with the capacitance prediction in EIS. Generally, based on the assumption of a uniform passive film with few defects, its corrosion resistance is positively correlated with its thickness [35,37,43]. In EIS testing, assuming the capacitance is constant, the passive film thickness increases with the increase of its exposed area which is positive related to the defects (see Fig. 12(d)). However, such increased thicker oxide film is not compact, larger thickness does not necessarily mean a better corrosion resistance.

3.4. XPS analysis

AES analysis demonstrate that outer layer of the L-PBF NiTi is mainly Ti- oxides and the inner layer is mainly Ni-oxides, the passive film thickness of three L-PBF NiTi is between 8.5 and 13.8 nm. In order to quantitatively analyze the difference between the two layers, we also analyzed the chemical composition of the outer layer of the original passive film and the inner layer after sputtering 6 nm. Fig. 13 shows the XPS element composition analysis of the passive films of three L-PBF NiTi samples immersed in 0.9 wt.% NaCl solution for 7
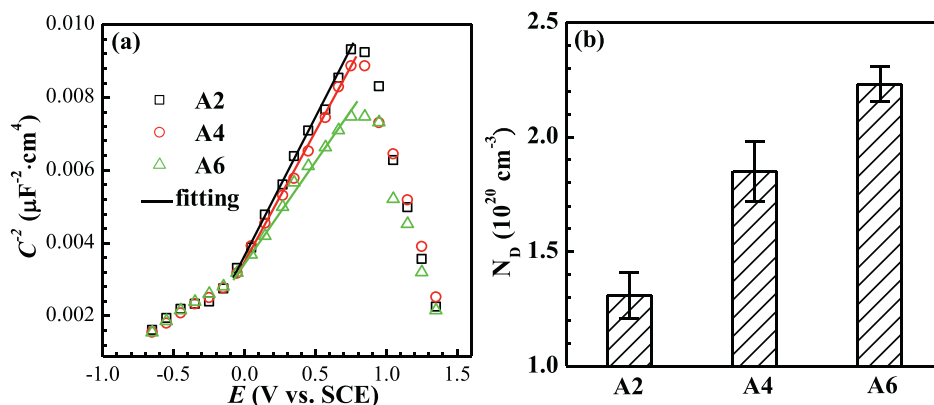
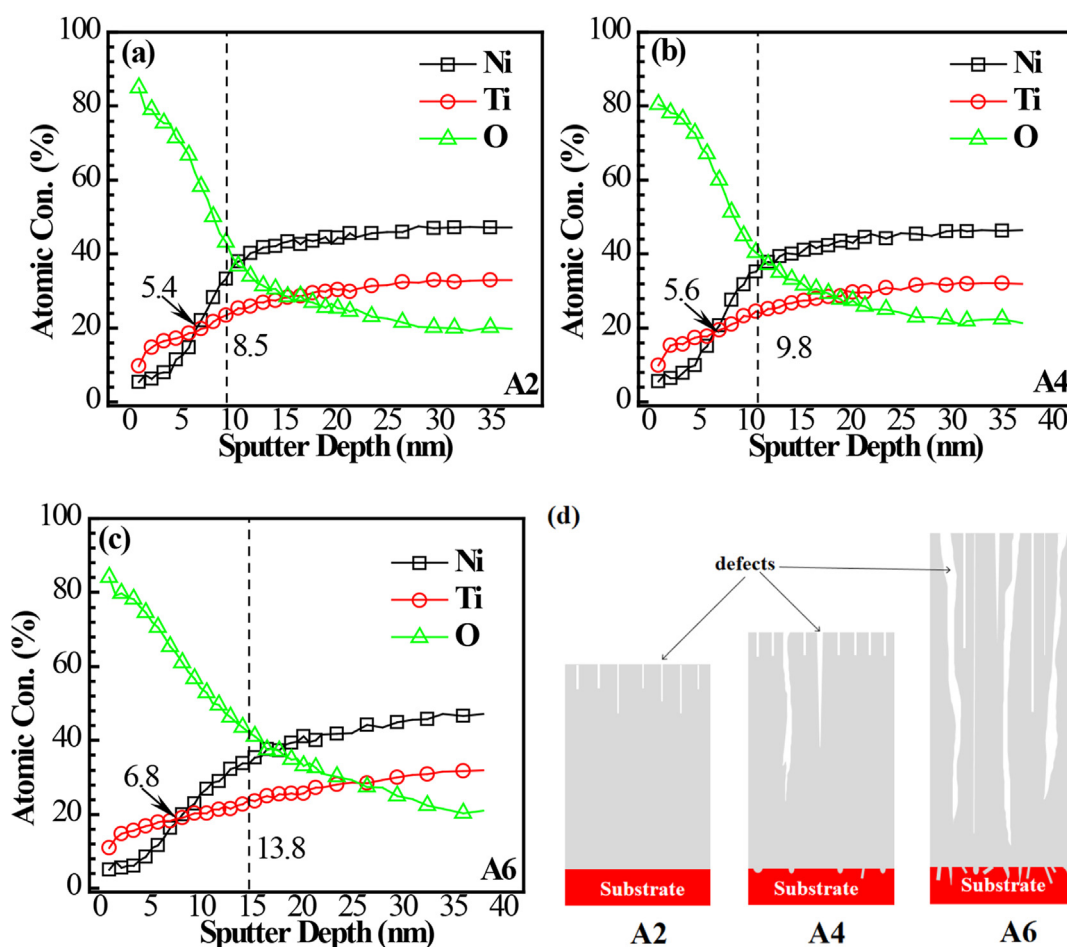Fig. 11 – Mott–Schottky curves (a) and N_D(b) of L-PBF NiTi after immersed in 0.9 wt.% NaCl solution for 7 days, A2 (56 J/mm³), A4 (87 J/mm³) and A6 (60 J/mm³).

Fig. 12 – AES of L-PBF NiTi after immersed in 0.9 wt.% NaCl solution for 7 days. (a) A2 (56 J/mm³), (b) A4 (87 J/mm³), (c) A6 (60 J/mm³), (d) the schematic diagram of the difference between the passive films of A2, A4 and A6.

days. As can be seen from the full spectrum in Fig. 12(a)–(c), the outer layer of the passive films of the three L-PBF NiTi are mainly composed of Ti and O, and obvious Ni peak could be detected in the inner layer of the passive films.

The peak value of the binding energy listed in Table 6 [44–46] is used for L-PBF NiTi component fitting. Fig. 13(a₁) - (c₁) shows the oxide composition of Ni 2p₃/₂ in the inner and

outer layers of the passive film. In the outer passive films of A2 and A4, only a very weak Ni (met) (852.8 eV) peak could be detected, while in A6 samples, weak Ni peak could be observed, which is mainly represented by two peaks: Ni (met) and NiO (853.7 eV). However, obvious Ni elements could be observed in the inner layer of the passive film of L-PBF NiTi. Ni is mainly Ni (met) and NiO. The content of Ni (met) is relatively

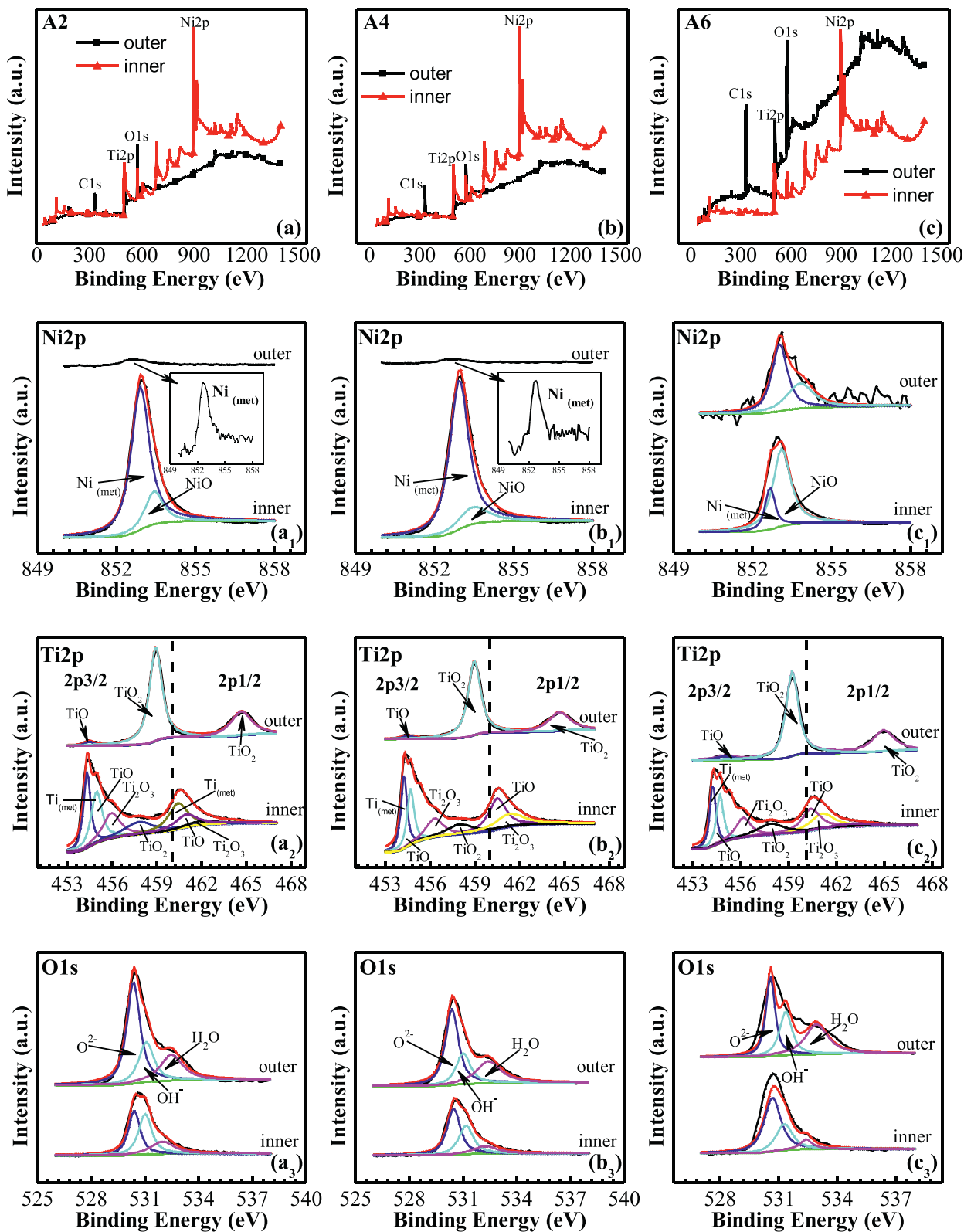Fig. 13 − XPS peaks comparison of L-PBF NiTi after immersed in 0.9 wt.% NaCl solution for 7 days. (a), (a$_1$), (a$_2$) and (a$_3$): A2 (56 J/mm^3); (b), (b$_1$), (b$_2$) and (b$_3$): A4 (87 J/mm^3); (c), (c$_1$), (c$_2$) and (c$_3$): A6 (60 J/mm^3).

Table 6 — Binding energies of major oxides peak values of L-PBF NiTi in passive film.

Element	Peak	Species/binding energy (eV)
Ti	$2p_{3/2}$	Ti (met)/454.1; TiO/454.6; Ti_2O_3/456.8; TiO_2/458.8
	$2p_{1/2}$	Ti (met)/460.1; TiO/460.2; Ti_2O_3/462.0; TiO_2/464.3
Ni	$2p_{3/2}$	Ni (met)/852.6; NiO/853.7; $Ni(OH)_2$/856.2
O	$1S$	O^{2-}/530.2; OH^-/531.8; H_2O/533

(454.6 eV) could also be detected, which again confirms that the outer passive film is mainly TiO_2. The content of TiO_2 in the inner passive film layer is significantly reduced, large numbers of low-priced Ti-oxides could be observed. Through first-principles calculation, Juan et al. [47] also showed that Ti^{4+} is mainly in the out layer of the passive film, Ti^{3+} species are present in the inner passive film. A2 contains a small amount of TiO_2 $2p_{3/2}$ (458.8 eV), Ti (met) $2p_{3/2}$ (454.1 eV), Ti (met) $2p_{1/2}$ (460.1 eV), TiO $2p_{3/2}$ (454.6 eV), TiO $2p_{1/2}$ (460.2 eV), Ti_2O_3 $2p_{3/2}$ (456.8 eV) and Ti_2O_3 $2p_{1/2}$ (462.0 eV). The Ti element distribution of A4 and A6 is similar to that of A2, in which the content of Ti (met) decreases, while the content of TiO and Ti_2O_3 increases. It can also be seen from Fig. 14 that Ti is mainly enriched in the outer layer of the passive film for A2 and A4, although the high-priced state Ti-oxides decreases in the inner passive film, the content of Ti in the total cation of passive film remains high, which is very beneficial to the corrosion resistance [48]. However, the content of Ti in the inner layer of A6 is higher than that of in the outer layer, which could attribute to the large number of defects in the passive film where Ti-oxide could be more easily detected.

high in A2 and A4 samples, and the amount of NiO is increased in A6 samples. It can also be seen from Fig. 12 that Ni is mainly enriched in the inner layer of the passive film, and the higher Ni content in the outer layer of A6 passive film may be related to the defects on its passive film. As the content of NiO in the inner layer increases, the total amount of Ni is decreased.

Fig. 13(a_2) - (c_2) shows the oxide composition of Ti in the inner and outer layers of the passive film. The outer passive films of the three L-PBF NiTi are mainly TiO_2 $2p_{3/2}$ (458.8 eV) and TiO_2 $2p_{1/2}$ (464.3 eV), and a small amount of TiO $2p_{3/2}$

Fig. 14 — (a) XPS element content comparison and (b) composition of the inner and outer layers of passive film of L-PBF NiTi after immersed in 0.9 wt.% NaCl solution for 7 days, taking A2 (56 J/mm^3) as an example.
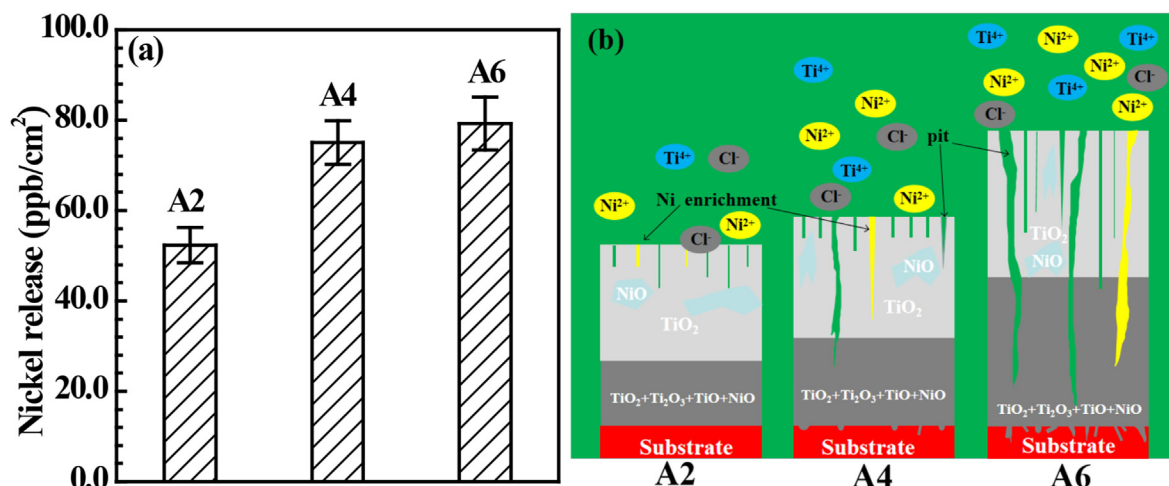

Fig. 15 — The Ni ion release concentration of L-PBF NiTi in 0.9 wt.% NaCl for 7days (a) and corrosion mode of Ni ion release on the three L-PBF NiTi passive film (b), A2 (56 J/mm^3), A4 (87 J/mm^3) and A6 (60 J/mm^3).

Fig. 13(a_3) - (a_3) shows the composition of O element in three L-PBF NiTi passive film. The O element is mainly composed of O^{2-} (530.2 eV), OH^- (531.8 eV) and H_2O (533 eV). The content of O^{2-} is the highest, which can be conformed to the Ti- oxides (TiO, Ti_2O_3, TiO_2) and Ni-oxide (NiO) formation in the passive film.

3.5. Ni ion release rate

NiTi-SMA is widely used in the medical field due to its excellent physical, mechanical and biological properties. However, NiTi-SMA contains nearly 50 at.% nickel, which is one of the biologically toxic elements, leading to inflammatory or allergic reactions of organisms, cell aberration and even carcinogenesis [6,8,17], so the release rate of Ni ions is also taken as an important evaluation criterion. Fig. 15(a) exhibits the Ni ion release concentration of the three L-PBF NiTi immersed in 0.9 wt.% NaCl solution for 7 days. The average value of the Ni ions release concentration of A2, A4 and A6 is 52.4, 74.9 and 79.3 ppb/cm^2, respectively, which is comparable to those reported by Briceño et al. [49], Zhang et al. [50] and Shabalovskaya et al. [51] that the one-week Ni ions release rate of NiTi-SMA ranges from 50 to 300 ppb/cm^2. Obviously, the Ni ions release rate of the three L-PBF NiTi is within the range of low values (50 ppb/cm^2) reported in the literature, among which A2 is very close to the lowest limit.

The difference in Ni ions release rate between the three L-PBF NiTi can be explained by the following model as shown in Fig. 15(b). Based on the previous electrochemical (see Figs. 4—8) and surface analysis (see Figs. 12—14), an outer TiO_2 rich and defect containing passive film could be formed on the surface of L-PBF NiTi after immersion in 0.9 wt.% NaCl solution. Ni ions will preferentially dissolve and release at the defect in the passive film [52]. As can be seen from the EIS test results in Fig. 10, the R_b of A2 in the range of $10^{5.8}$ Ω cm^2 has the best corrosion resistance. However, the R_b of A4 and A6 passive film decreased by an order of magnitude ($10^{4.8}$—$10^{4.9}$ Ω cm^2), indicating that there are a large number of defects in the passive film. Although the AES (see Fig. 12) results demonstrate relatively thick passive film of A4 and A6, the film contains a high density of defects and therefore cannot effectively prevent the release of Ni ions. A6, which has the maximum numbers of crack and keyhole defects, shows the highest Ni ion release rate. In addition to electrochemical test, immersion test is also a commonly used method to investigate the corrosion performance for biomedical applications, especially under the conditions of corrosion and mechanical coupling [53,54]. Although the results of present work showed that A2, prepared by L-PBF exhibited excellent corrosion resistance and lowest Ni ion release rate, more tests are still needed to confirm the feasibility of its clinical application.

4. Conclusions

The corrosion behavior of three additively manufactured NiTi alloys fabricated by L-PBF with various E_v (A2 (56 J/mm^3), A4 (87 J/mm^3) and A6 (60 J/mm^3)) was systematically investigated by means of electrochemical testing surface analysis and combined with ICP-MS in 0.9 wt% NaCl solution. The main conclusions are as follows.

(1) The defects at the alloy surface can promote the passive film formation rate during early stages of exposure. A corrosion resistant passive film could be formed on the surface of A2 with barrier resistance value in the order $10^{5.8}$ Ω cm^2 after immersion for 6 h. The corrosion resistance of L-PBF NiTi from high to low is: A2 > A4 > A6.

(2) The L-PBF NiTi passive films show a two-layer structure with an outer Ti- rich (TiO_2) layer and inner Ni- and Ti-rich layer. The passive film thickness of the L-PBF NiTi ranges from 8.5 nm to 13.8 nm and increases with the amount of defects in the order of A2 < A4 < A6.

(3) The Ni ion release rate of the L-PBF NiTi range from 52.4 to 79.3 ppb/cm^2, and is in the order of A2 < A4 < A6. The release rate of A2 is close to the lowest value of commercial NiTi alloys (50—300 ppb/cm^2) in the literature.

(4) A2, prepared by L-PBF with linear energy density of 0.2 J/m and volumetric energy density of 56 J/mm^3 has the most uniform surface morphology, the best passive film corrosion resistance and the lowest Ni ion release rate.

CRediT author statement

Ming Liu: Conceptualization, Methodology, Investigation, Writing — original draft. **Jianing Zhu**: Resources, Investigation, Writing — review & editing. **V.A. Popovich**: Resources, Methodology, Validation, Supervision, Writing — review & editing. **E. Borisov**: Resources, Methodology, Validation. **J.M.C. Mol**: Methodology, Validation, Supervision, Writing — review & editing. **Y. Gonzalez-Garcia**: Methodology, Validation, Supervision, Writing — review & editing.

Declaration of Competing Interest

The authors declare that they have no known competing financial interests or personal relationships that could have appeared to influence the work reported in this paper.

Acknowledgments

REFERENCES

[1] Envelope HADP, Garcia E, Murillo-Marrodán A. Effects of tool—workpiece interfaces friction coefficient on power and energy consumption during the piercing phase of seamless tube production. J Mater Res Technol 2022;19:3172—88.

[2] Yu ZL, Xu ZH, Guo YT, Xin RL, Liu RY, Jiang CR, et al. Study on properties of SLM-NiTi shape memory alloy under the same energy density. J Mater Res Technol 2021;13:241–50.

[3] Zhu X, Chu L, Dui G. Constitutive modeling of porous shape memory alloys using Gurson–Tvergaard–Needleman model under isothermal conditions. Int J Appl Mech 2020;12(3):2050038.

[4] Say Y, Aksakal B. Enhanced corrosion properties of biological NiTi alloy by hydroxyapatite and bioglass based biocomposite coatings. J Mater Res Technol 2020;9(2):1742–9.

[5] Wang B, Kang GZ, Kan QH, Wu WP, Zhou K, Yu C. Atomistic study on the super-elasticity of single crystal bulk NiTi shape memory alloy under adiabatic condition. Comput Mater Sci 2018;142:38–46.

[6] Phukaoluan A, Khantachawana A, Kaewtatip P, Dechkunakorn S. Assessment of corrosion behavior in artificial saliva of wires for orthodontic applications. Mater Sci Forum 2018;917:197–201.

[7] Shanaghi A, Chu PK. Enhancement of mechanical properties and corrosion resistance of NiTi alloy by carbon plasma immersion ion implantation. Surf Coating Technol 2018;365:52–7.

[8] Liu M, Li J, Zhang YX, Xue YN. Recent Advances in corrosion research of biomedical NiTi shape Memory alloy. Rare Met Mater Eng 2021;50(11):4165–73.

[9] Velmurugan C, Senthilkumar V, Kamala PS. Microstructure and corrosion behavior of NiTi shape memory alloys sintered in the SPS process. Int J Miner Metall Mater 2019;26(10):1311–21.

[10] Shanaghi A, Chu PK. Investigation of corrosion mechanism of NiTi modified by carbon plasma immersion ion implantation (C-PIII) by electrochemical impedance spectroscopy. J Alloys Compd 2019;790:1067–75.

[11] Wang H, Juergensen J, Decker P, Hu ZY, Yan K, Gurevich EL, et al. Corrosion behavior of NiTi alloy subjected to femtosecond laser shock peening without protective coating in air environment. Appl Surf Sci 2020;501(31):144338.

[12] Mirjalili M, Momeni M, Ebrahimi N, Moayedet MH. Comparative study on corrosion behaviour of Nitinol and stainless steel orthodontic wires in simulated saliva solution in presence of fluoride ions. Mater Sci Eng C 2013;33(4):2084–93.

[13] Mocnik P, Kosec T, Kovac J, Bizjak M. The effect of pH, fluoride and tribocorrosion on the surface properties of dental archwires. Mater Sci Eng C 2017;78:682–9.

[14] Ogawa CM, Faltin K, Maeda FA, Ortolani CLF, Guaré RO, Cardosoet CAB. In vivo assessment of the corrosion of nickel–titanium orthodontic archwires by using scanning electron microscopy and atomic force microscopy. Microsc Res Tech 2020;83(8):928–36.

[15] Figueira N, Silva TM, Carmezim MJ, Carmezim MJ, Fernandes JCS. Corrosion behaviour of NiTi alloy. Electrochim Acta 2009;54(3):921–6.

[16] Dong P, Yao R, Yan Z, Yan Z, Wang W, He X, et al. Microstructure and corrosion resistance of laser-welded crossed nitinol wires. Materials 2018;11(5):842.

[17] Elahinia M, Moghaddam NS, Andani MT, Amerinatanzi A, Bimber BA, Hamilton RF. Fabrication of NiTi through additive manufacturing: a review. Prog Mater Sci 2016;83:630–63.

[18] Chen X, Liu K, Guo W, Gangil N, Siddiquee AN, Konovalov S. The fabrication of NiTi shape memory alloy by selective laser melting: a review. Rapid Prototyp J 2019;25(8):1421–32.

[19] Wang C, Tan XP, Du Z, Chandra S, Sun Z, Lim CWJ, et al. Additive manufacturing of NiTi shape memory alloys using pre-mixed powders. J Mater Process Technol 2019;271:152–61.

[20] Zhong K, Yong L, Jia A, Chua CK, Shen YF, Kuo CN. A review of selective laser melted NiTi shape memory alloy. Materials 2018;11(4):519.

[21] Marattukalam JJ, Singh AK, Datta S, Das M, Balla VK, Bontha S, et al. Microstructure and corrosion behavior of laser processed NiTi alloy. Mater Sci Eng C 2015;57:309–13.

[22] Zhu JN, Borisov E, Liang X, Farber E, Hermans MJM, Popovich VA. Predictive analytical modelling and experimental validation of processing maps in additive manufacturing of nitinol alloys. Addit Manuf 2021;(38):101802.

[23] Haleem SMAE, Aal EEAE, Wanees SAE, Diabet A. Environmental factors affecting the corrosion behaviour of reinforcing steel: I. The early stage of passive film formation in Ca(OH)$_2$ solutions. Corrosion Sci 2010;52(12):3875–82.

[24] Liu M, Cheng XQ, Li XG, Pan Y, Li J. Effect of Cr on the passive film formation mechanism of steel rebar in saturated calcium hydroxide solution. Appl Surf Sci 2016;389(15):1182–91.

[25] Fischer H, Hauffe K. Passivierende filme und Deckschichten Anlaufschichten. Springer; 1956.

[26] Liu M, Cheng XQ, Zhao GC, Li XG, Pan Y. Corrosion resistances of passive films on low Cr steel and Carbon steel in simulated concrete pore solution. Surf Interface Anal 2016;48:981–9.

[27] Yang XJ, Du CW, Wan HX, Liu ZY, Li XG. Influence of sulfides on the passivation behavior of titanium alloy TA2 in simulated seawater environments. Appl Surf Sci 2018;458:198–209.

[28] Roger P. Atlas of electrochemical equilibria in aqueous solutions. J Electroanal Chem 1967;13(4):471.

[29] Ayoub H, Griveau S, Lair V, Brunswick P, Cassir M, Bediouiet F. Electrochemical characterization of nickel electrodes in phosphate and carbonate electrolytes in view of assessing a medical diagnostic device for the detection of early diabetes. Electroanalysis 2010;22(21):2483–90.

[30] Wang Y, Cheng XQ, Li XG. Electrochemical behavior and compositions of passive films formed on the constituent phases of duplex stainless steel without coupling. Electrochem Commun 2015;57:56–60.

[31] Milosev I, Kosec T. Study of Cu-18Ni-20Zn Nickel Silver and other Cu-based alloys in artificial sweat and physiological solution. Electrochim Acta 2007;52:6799–810.

[32] Liu M, Cheng XQ, Li XG, Zhou C, Tan HL. Effect of carbonation on the electrochemical behavior of corrosion resistance low alloy steel rebars in cement extract solution. Construct Build Mater 2016;130(15):193–201.

[33] Taheri P, Miloev I, Meeusen M, Kapun B, White P, Kokalj A, et al. On the importance of time-resolved electrochemical evaluation in corrosion inhibitor-screening studies. npj Mater Degrad 2020;4:12.

[34] Chen G, Wen S, Ma J, Sun ZY, Lin CG, Yue ZF, et al. Optimization of intrinsic self-healing silicone coatings by benzotriazole loaded mesoporous silica. Surf Coating Technol 2021:127388.

[35] Sun XT, Kang ZX, Zhang XL, Jiang HJ, Guan RF, Zhang XP. A comparative study on the corrosion behavior of porous and dense NiTi shape memory alloys in NaCl solution. Electrochim Acta 2011;56(18):6389–96.

[36] Chembath M, Balaraju JN, Sujata M. Surface characteristics, corrosion and bioactivity of chemically treated biomedical grade NiTi alloy. Mater Sci Eng C 2015;56:417–25.

[37] Freitag M, Osiewicz B, Goryczka T, Lelątko J. Application of EIS to study the corrosion resistance of passivated NiTi shape memory alloy in simulated body fluid. Solid State Phenom 2012;183:57–64.

[38] Wang R, Luo SJ, Liu M, Xue YN. Electrochemical corrosion performance of Cr and Al alloy steels using a J55 carbon steel as base alloy. Corrosion Sci 2014;85:270—9.

[39] Liu M, Cheng XQ, Li XG, Lu TJ. Corrosion behavior of low-Cr steel rebars in alkaline solutions with different pH in the presence of chlorides. J Electroanal Chem 2017;803(15):40—50.

[40] Barros C, Gomes J. Strain induced localized corrosion of NiTi, NiTiCo and NiTiCr alloys in 0.9% NaCl. J Mech Behav Biomed Mater 2020;112:104015.

[41] Qiu P, Gao PP, Wang SY, Li ZH, Wang Y, Zhang QQ, et al. Study on corrosion behavior of the selective laser melted NiTi alloy with superior tensile property and shape memory effect. Corrosion Sci 2020;175(11):108891.

[42] Lv JL, Liang TX, Wang C, Dong LM. Surface corrosion enhancement of passive films on NiTi shape memory alloy in different solutions. Mater Sci Eng C 2016;63:192—7.

[43] Luo H, Su H, Dong CF, Xiao K, Li XG. Electrochemical and passivation behavior investigation of ferritic stainless steel in alkaline environment. Construct Build Mater 2015;96:502—7.

[44] Alqarni ND, Wysocka J, El-Bagoury N, Ryl J, Amin MA, Boukherroub R. Effect of cobalt addition on the corrosion behavior of near equiatomic NiTi shape memory alloy in normal saline solution: electrochemical and XPS studies. RSC Adv 2018;8(34):19289—300.

[45] Rudolf R, Stamboli A, Kocijan A. Atomic layer deposition of aTiO$_2$ layer on nitinol and its corrosion resistance in a simulated body fluid. Metals 2021;11:659.

[46] Yang X, Yang Y, Sun M, Jia JH, Cheng XQ, Pei ZB, et al. A new understanding of the effect of Cr on the corrosion resistance evolution of weathering steel based on big data technology. J Mater Sci Technol 2022;104:67—80.

[47] Juan J, Orazi V, Sandoval M, Bechthold P, Hernández-Laguna A, Sainz-Díaz CI, et al. DFT study of Ni segregation at the B2-NiTi(110)/rutile-TiO$_2$(110) interface. Appl Surf Sci 2019;489:287—96.

[48] Wang L, Yu HY, Wang SY, Chen B, Wang YH, Fan WQ, et al. Quantitative analysis of local fine structure on diffusion of point defects in passive film on Ti. Electrochim Acta 2019;314(12):161—72.

[49] Brice NJ, Romeu A, Espinar E, Llamas JM, Gil FJ. Influence of the microstructure on electrochemical corrosion and nickel release in NiTi orthodontic archwires. Mater Sci Eng C 2013;33(8):4989—93.

[50] Zhang C, He WL, Chen YM, Dai DN, Su Y, Shao LQ. Corrosion behavior and in vitro cytotoxicity of Ni—Ti and stainless steel arch wires exposed to lysozyme, ovalbumin, and bovine serum albumin. ACS Omega 2020;5(30):18995—9003.

[51] Shabalovskaya SA, Tian H, Anderegg JW, Schryvers DU, Carroll WU, Humbeeck JV. The influence of surface oxides on the distribution and release of nickel from Nitinol wires. Biomaterials 2009;30(4):468—77.

[52] Asserghine A, Medvidović-Kosanović M, Nagy L, Nagy G. In situ monitoring of the transpassivation and repassivation of the passive film on nitinol biomaterial by scanning electrochemical microscopy. Electrochem Commun 2019;107:106539.

[53] Shuai C, Wang B, Yang Y, Peng SP, Gao CD. 3D honeycomb nanostructure-encapsulated magnesium alloys with superior corrosion resistance and mechanical properties. Compos B Eng 2019;162:611—20.

[54] Lu P, Wu M, Liu X, Duan WP, Han JT. Study on corrosion resistance and bio-tribological behavior of porous structure based on the SLM manufactured medical Ti6Al4V. Met Mater Int 2020;26(8):1182—91.